

Application of time series based damage detection algorithms to the benchmark experiment at the National Center for Research on Earthquake Engineering (NCREE) in Taipei, Taiwan

Hae Young Noh, K. Krishnan Nair and Anne S. Kiremidjian

Department of Civil and Environmental Engineering, Stanford University, Stanford, CA 94305, USA

C-H. Loh

National Taiwan University, Taipei, Taiwan

(Received November 27, 2007, Accepted September 1, 2008)

Abstract. In this paper, the time series based damage detection algorithms developed by Nair, *et al.* (2006) and Nair and Kiremidjian (2007) are applied to the benchmark experimental data from the National Center for Research on Earthquake Engineering (NCREE) in Taipei, Taiwan. Both acceleration and strain data are analyzed. The data are modeled as autoregressive (AR) processes, and damage sensitive features (*DSF*) and feature vectors are defined in terms of the first three AR coefficients. In the first algorithm developed by Nair, *et al.* (2006), hypothesis tests using the *t*-statistic are applied to evaluate the damaged state. A damage measure (*DM*) is defined to measure the damage extent. The results show that the *DSF*'s from the acceleration data can detect damage while the *DSF* from the strain data can be used to localize the damage. The *DM* can be used for damage quantification. In the second algorithm developed by Nair and Kiremidjian (2007) a Gaussian Mixture Model (GMM) is used to model the feature vector, and the Mahalanobis distance is defined to measure damage extent. Additional distance measures are defined and applied in this paper to quantify damage. The results show that damage measures can be used to detect, quantify, and localize the damage for the high intensity and the bidirectional loading cases.

Keywords: structural health monitoring; damage diagnosis; autoregressive model; hypothesis test; Gaussian mixture model.

1. Introduction

Over the past decade statistical pattern recognition methods for structural damage diagnosis have been successfully applied to simulated and laboratory experimental data. The data that are available for validation and calibration of these methods, however, have been very limited. Recognizing the need for additional data from experiments whereby damage is introduced in a systematic and controlled way has led to a series of laboratory test. In this paper, the time series based damage detection algorithms developed by Nair, *et al.* (2006) and Nair and Kiremidjian (2007) are applied to the data obtained from the benchmark experiment conducted at the National Center for Research on Earthquake Engineering

(NCREE) in Taipei, Taiwan (Lynch, *et al.* 2006). The algorithm is based on the premise that structural damage will change the vibration response of the structure. While previous validation and calibration tests with this algorithm have involved only acceleration measurements, in this paper both acceleration and strain data are used to evaluate the robustness of the algorithm. The algorithm involves the modeling of vibration and strain signals as autoregressive (AR) processes. The first three AR coefficients of the model are used to define the feature vector which serves as the diagnostic tool for damage identification. As shown by Nair, *et al.* (2006) these coefficients are directly related to the mode shapes and frequencies of the structure and thus can be used to capture changes in these structural properties. The feature vectors are used in two different algorithms for damage diagnosis. In the first algorithm, which follows Nair, *et al.* (2006), a damage sensitive feature (*DSF*) is defined as a function of the first three AR coefficients. Hypothesis tests using the t-statistic are applied to discriminate a damaged state from an undamaged one. A damage measure (*DM*) is defined in terms of the mean values and the standard deviation of the *DSF*'s to measure the extent of the damage. In the second algorithm, which follows the developments of Nair and Kiremidjian (2007) a Gaussian Mixture Model (GMM) is used to model the feature vector. Damage diagnosis is achieved by determining the distance between mixtures. The Mahalanobis distance, which is defined as the Euclidean distance between the mixtures weighted with respect to the inverse covariance matrix, as well as various distance measures are used to detect damage and measure damage extent. In the following sections, a description of the NCREE experimental benchmark test is presented, and the data that are used in the application of the algorithm are described. Then the two models are applied to the data. It is shown that the algorithms are able to identify damage in majority of the cases. Damage extent and location, however, are not always well represented by these measures.

2. Description of experiment

An experiment was designed and performed at the National Center for Research on Earthquake Engineering (NCREE) in Taipei, Taiwan in order to provide information on a controlled damage occurrence on a structure. For that purpose, a three story single bay steel frame (Fig. 1) was constructed and various sensors were deployed at different locations on the benchmark structure. The inter story height of the benchmark structure is 3 m. Floor dimensions at every story are 3 m \times 2 m, and each floor mass is 6 tons. H150 \times 150 \times 7 \times 10 steel I-beams are used for the beams and the columns, and each beam-column joint is designed as a bolted connection (Lynch, *et al.* 2006).

The excitation on the benchmark structure is applied through a shaking table representing ground motions. Random excitations with maximum amplitudes of 60 gal intensity in the X-direction, 100 gal intensity in the X-direction, and 50 gal intensity in the XY-direction were applied. In addition, selected strong ground motions from the 1940 El Centro, California, 1995 Kobe, Japan, and the 1999 Chi-Chi, Taiwan, records were applied to the structure. Both wired and wireless sensors were installed on the structure. These included accelerometers and strain gauges. The data from only wired sensors are used for analysis in this paper. Data were collected at 200 Hz sampling rate. Fig. 1 shows the location of the deployed sensors on the benchmark structure. In this figure, A and S represent acceleration and strain sensors, respectively. In this paper, we use the measurements from both sensors with the unidirectional and bidirectional random excitations. Data from all locations were considered; however, not all data could be used because some of the data were corrupted. For each excitation with 50 gal, 60 gal, and 100 gal intensities, acceleration data were collected from 12 different locations, and strain data were

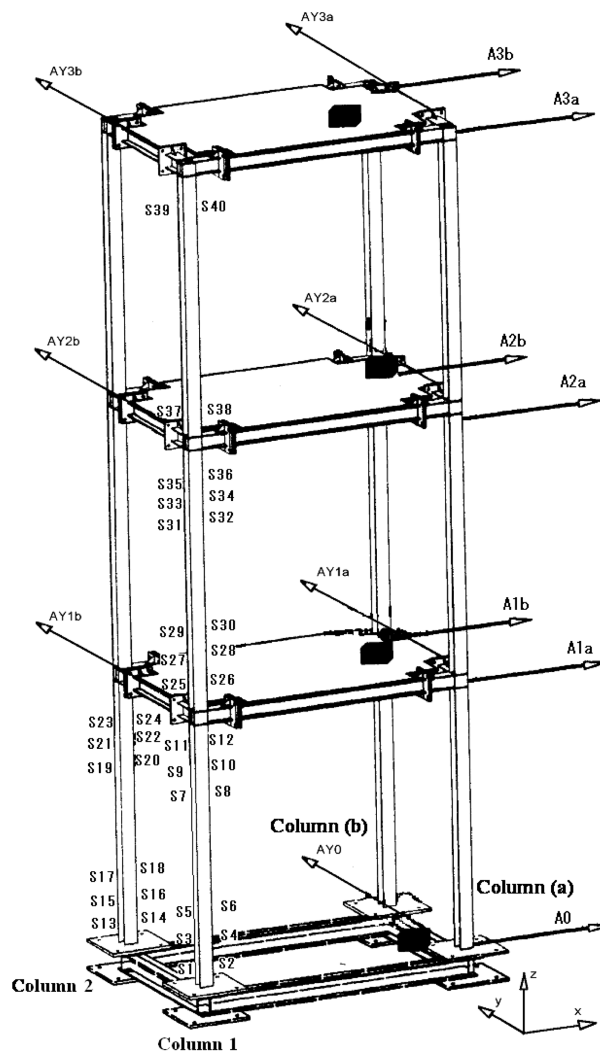


Fig. 1 Benchmark structure and sensor locations used at the NCREE test

collected from 40 different locations for each damage state. Table 1 shows all the data that were collected, identifies how many records were corrupted and how many were used in the analysis presented in this paper.

In order to compare the behavior of the structure from a normal condition to damaged conditions, two damage cases were introduced during the experiment. In the first damage case the flanges at the lower part of column 1 (Fig. 1) at the ground floor were reduced in width by 26.67% (Fig. 2). The second damage case has the flanges of both columns 1 and 2 cut the same amount near the ground floor. Hereafter we will refer to these as DP1 and DP2, respectively. Fig. 2 shows the damage that was introduced to the base columns.



Fig. 2 Photograph of the cut flanges of the column

3. Description of algorithm

The autoregressive (AR) model is used in this paper to define two algorithms for damage identification, quantification, and localization. For this purpose AR coefficients are computed from the data for the undamaged and damaged structure, and the two signals are analyzed. We briefly summarize the two algorithms that will be used in the analysis of the data.

In the first algorithm a damage sensitive feature, *DSF*, is defined based on the AR coefficients. To compare the two signals, the *DSF* is tracked as damage is incurred. Thus, the selection of the *DSF* is very important and has to reflect the physical properties of the structure. A relationship between the structural modes and frequencies and the first three AR coefficients was developed by Nair, *et al.* (2006) demonstrating that indeed these coefficients are suitable for damage discrimination. The algorithm developed by Nair, *et al.* (2006) consists of three steps (i) time series modeling of vibration signal, (ii) damage sensitive feature extraction, and (iii) statistical classification using the t-test for predicting damage.

Modeling of the vibration signal includes the removal of trends, obtaining the optimal model order and checking the assumptions of the residuals of the AR model. To extract the appropriate *DSF*, an AR model is fitted to the data and different forms of the *DSF* based on the AR coefficients are considered. Statistical analysis is performed on the *DSF* values for the pre and post damage signals as a tool for change detection, and the significance of that change is tested by various statistical techniques.

The algorithm is performed in the following steps assuming that all preprocessing has already been completed:

- Obtain signals from an undamaged structure, from sensor i , denoted by $x_i(t)$ ($i = 1, \dots, N$), where N is the number of sensors. Segment the signal x_i into chunks of finite duration, $x_{ij}(t)$ ($j = 1, \dots, M$), where M is the number of chunks. Populate a database with these baseline signals.
- Standardize and normalize the signal $x_{ij}(t)$ to remove all trends and environmental conditions to obtain $\tilde{x}_{ij}(t)$.
- Obtain signals from a potentially damaged structure for the same sensor, denoted by $z_i(t)$, ($i = 1, \dots, N$). As in the previous steps, segment $z_i(t)$ into $z_{ij}(t)$ ($j = 1, \dots, M$) and then standardize and normalize it to obtain $\tilde{z}_{ij}(t)$.
- Fit an AR model to the signals $\tilde{x}_{ij}(t)$ and $\tilde{z}_{ij}(t)$ for all i and j .
- For each sensor i , define and compute the statistics of the damage sensitive feature, *DSF*, for each

chunk in the pre- and post-event signals. Compute the mean and pooled variance of the DSF for the pre- and post-event signals.

- Determine the statistical significance in the differences of mean values of the pre- and post- event data using the t-test to report the damage decision at sensor i .
- Calculate the damage measure DM for each sensor.

The second damage identification algorithm used in this paper was developed by Nair and Kiremidjian (2007). The steps in this algorithm are as follows: (i) time series modeling of vibration signal, (ii) modeling of feature vectors using Gaussian Mixture Models, GMMs, and (iii) using the Mahalanobis distance to determine the damage extent.

In this algorithm, the first three AR coefficients of the signals are defined as the feature vectors. The feature vectors are modeled as GMMs. The pre and post damage signals are assumed to be from different Gaussian mixtures, and the parameters of the GMMs are calculated. The parameters of the GMM are the mean value vector and covariance matrix of the variables. The Mahalanobis distance between the mixtures is measured to determine the damage state. A brief summary of the formulations for each model is presented in the following sections as they apply to the data obtained from the NTU steel frame test.

3.1. Time series modeling of vibration signal

The first step of the analysis is to examine the data and eliminate corrupted signals or those signals that do not satisfy the requirements for AR modeling. The data could be corrupted due to faulty instrumentation, changes in environmental conditions, faulty sensors, or faulty transmission via cabling or via the wireless transmission, among the many possible alternatives. For example, signals that are non-stationary, or that do not appear to correspond to structural behavior, or data that are erratic need to be discarded. Figs. 3(a), and (b) show examples of corrupted signals. In Fig. 3(a) the signal is nonstationary showing increasing amplitude. In Fig. 3(b) the signal is jumping up and down showing that the sensor may be unstable or loose. Table 1 shows the total number of signals obtained from the test and the number of signals used for analysis for each case.

For the signals that appear to be appropriately collected by the sensors, the signals are segmented to form chunks. Each of these chunks is standardized and normalized using the following expression:

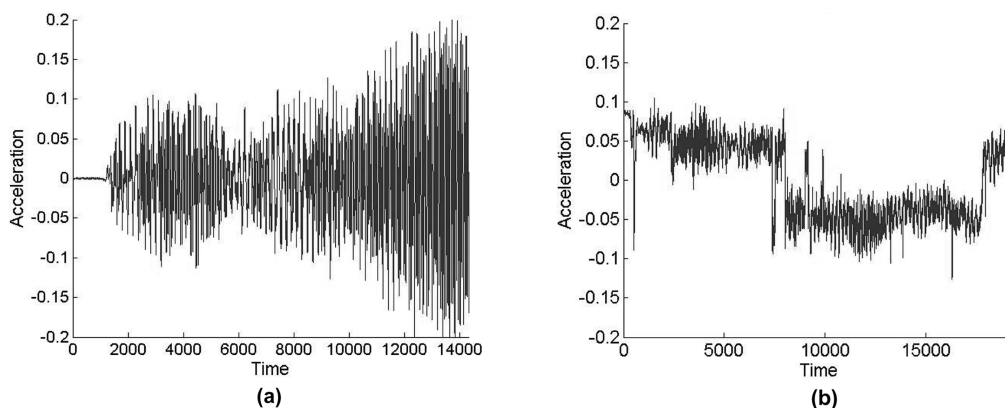


Fig. 3 Examples of corrupted data

Table 1 Number of data obtained and used for the analysis

		60 gal X-direction uni-directional random excitation		100 gal X-direction unidirectional random excitation		50 gal XY-direction bidirectional random excitation	
Direction		X	Y	X	Y	X	Y
Acceleration Data	Total	6	6	6	6	6	6
	Uncorrupted*	4	4	0	5	5	6
Strain Data (Z-direction)	Total	40		40		40	
	Uncorrupted*	35		38		39	

*Only the uncorrupted data are used for the analysis.

$$\tilde{x}_{ij}(t) = \frac{x_{ij}(t) - \mu_{ij}}{\sigma_{ij}} \quad (1)$$

where $x_{ij}(t)$ is the signal (acceleration or strain) obtained from sensor i and chunk j , μ_{ij} and σ_{ij} are the mean and standard deviation of the signal $x_{ij}(t)$ respectively. The tilde in the notation has been dropped for simplicity. Subtracting the mean value standardizes the signal to the same amplitudes and dividing by the standard deviation normalizes the signal to reduce the effect of local variability. This procedure is performed in order to compare signals (at a sensor location) that may have occurred due to different loading conditions (i.e. different magnitudes and directions of loads) and/or different environmental conditions.

After standardizing and normalizing the signal, time series models are fitted to these signals. Since the input motion is available, the ARX model is applied to fit the data. In addition, the AR model is also used as it is the simplest time series model available. The Burg and least squares algorithms are applied to obtain the AR/ARX coefficients, respectively (Brockwell and Davis 2002).

The ARX model is given by:

$$x_{ij}(t) = \sum_{k=1}^p \alpha_k x_{ij}(t-k) + \left(\sum_{k=1}^q \beta_k y_{ij}(t-k) \right) + \varepsilon_{ij}(t) \quad (2)$$

where $x_{ij}(t)$ is the normalized acceleration signal, $y_{ij}(t)$ is the normalized input signal, α_k and β_k are the k th AR and exogenous input coefficient respectively; p and q are the model orders of the AR and the exogenous input processes respectively and $\varepsilon_{ij}(t)$ is the residual term. Similarly the AR model is given by:

$$x_{ij}(t) = \sum_{k=1}^p \alpha_k x_{ij}(t-k) + \varepsilon_{ij}(t) \quad (3)$$

Note that the AR model is an ARX model with the exogenous input model order $q=0$.

The optimal order of AR and ARX model is selected using the Akaike Information Criteria (AIC). Figure 4 shows the variation of the values of AIC with AR model order for different input orders, q , of the ARX model for the data from the steel frame structure. It should be noted that when q is zero, the ARX model reduces to the simple AR model. It is observed that as the input model orders vary from $q = 0$ to 4, the AIC values are similar to those of AR model order p . Thus, the AR model is selected as the simplest model that captures the characteristics of the signal. For this study, an optimal AR model order of 7 is chosen for both acceleration and strain signals.

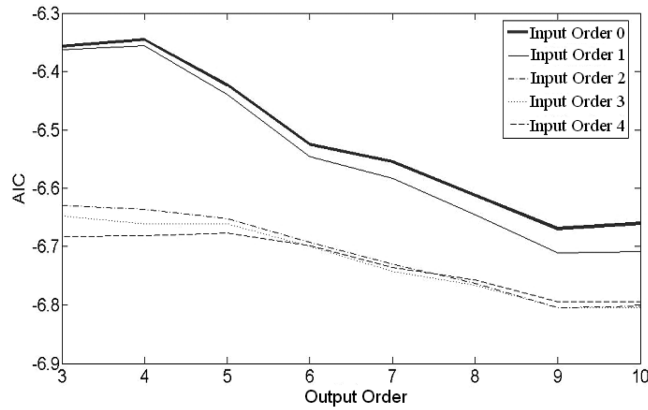


Fig. 4 Variation of AIC with model order

Table 2 Stability of the first AR coefficient

Points. per chunk	100	200	500	1000	1500
Mean	-1.5219	-1.5287	-1.5388	-1.5471	-1.5520
Std. deviation	0.0874	0.0811	0.0692	0.0578	0.0271
COV	-0.0574	-0.0531	-0.0376	-0.0279	-0.0174

The stability of the AR coefficients with chunk size of the signals obtained from the test is examined next. Each set of acceleration and strain data is divided into chunks of the same size for analysis. In order to determine the optimal chunk size (number of points in a segment), several sets of data are analyzed with different chunk sizes. For these data sets, the means and variances of the first AR coefficients are calculated. Table 2 shows the result of the analysis of the strain signal obtained at sensor 1 as identified in Fig. 1. The chunk sizes are selected such that the coefficient of variation (COV) of the AR coefficients is less than 0.1. Table 2 shows that a chunk size of 100 points has COV smaller than 0.1. Chunk sizes are varied by gradually increasing the number of points from 100 to 1500 and computing the statistics for each set. From Table 2 it can be observed that the mean value changes very slightly with increased chunk size, but the standard deviation as expected decreases. It is found, however, that with chunk sizes larger than 200, the COV is less than 0.05 (or 5%) which is considered to be an acceptable variation for the purposes of this analysis. Thus a chunk size of 200 points is used for the analysis.

Following the fitting of the AR model, the residuals are examined to determine if they are independent and identically distributed (iid) as required for AR modeling. For this purpose the variation with time, the normal probability plot, and the variation of the autocorrelation function with lag of the residuals are plotted for further examination. Figure 5(a) shows the variation of the residuals within a chunk of data for one signal. We can see that there are no trends, thus indicating homoskedasticity in the residuals. Figure 5(b) is the normal probability plot of the residuals. The residuals follow the straight line closely and start deviating at the ends, indicating that there is a slight deviation from normality only at the tails. Figure 5(c) shows the autocorrelation function (ACF) of the residuals. Since the ACF values are small and decrease with lag, it can be concluded that the residuals are stationary. Thus, all conditions for fitting an AR model have been satisfied.

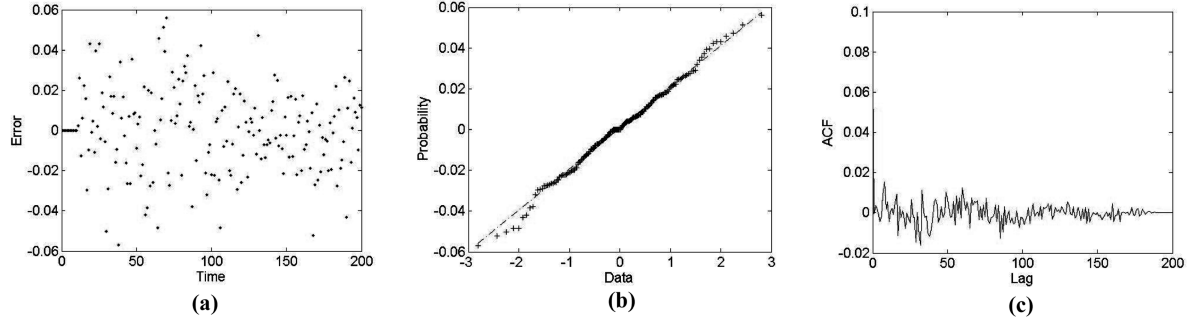


Fig. 5 Residuals diagnostics: (a) Variation of residuals with time; (b) Normal probability plot of the residuals; (c) Variation of ACF with lag

3.2. Algorithm 1

3.2.1. Feature extraction

After extensive investigation of various combinations of AR coefficients as candidates for damage measures, it was found that the first three coefficients can be used to define the damage sensitive feature (*DSF*). As stated in the introduction, Nair, *et al.* (2006) have shown that these coefficients are functionally related to the frequencies and mode shapes of a structure. Using the acceleration signal, two DSF_{acc} are defined as follows:

$$DSF_{acc,1} = \frac{\alpha_1}{\sqrt{\alpha_1^2 + \alpha_2^2 + \alpha_3^2}}$$

$$DSF_{acc,2} = \alpha_1 \quad (4)$$

where, α_i is the i^{th} AR coefficient. The *DSF* using strain data, DSF_{str} , is defined as the first AR coefficient α_1 .

The analysis for the *DSF* for the undamaged case, DP1, and DP2 at all sensor locations on the structure and for all loading conditions is performed following the algorithm described above. The mean *DSF* values are computed, and the t-test is used to determine the significance of the difference between them. We first present the results for selected sensor locations to illustrate the model. Fig. 6 shows the variation of *DSF* for the AR model that has detected damage. Fig. 6(a) is the plot of $DSF_{acc,2}$ for acceleration signal AY1b (as identified in Fig. 1) for random excitation in the X-direction having a peak acceleration of 100 gal. Fig. 6(b) illustrates the result for strain sensor S3 (as shown in Fig. 1) for random bidirectional excitation. In both cases, it is observed that the mean of the *DSF*'s for the undamaged case is less than that of DP1, which is in turn smaller than that of DP2.

A damage measure, *DM*, is defined in terms of the mean values and the standard deviation of the *DSF*'s as follows:

$$DM = \frac{(\mu_{DSF,u} - \mu_{DSF,d})^2}{\sigma_{DSF,u}^2} \quad (5)$$

DM is used to quantify the difference between the *DSF*'s for the undamaged case and those for the damaged case.

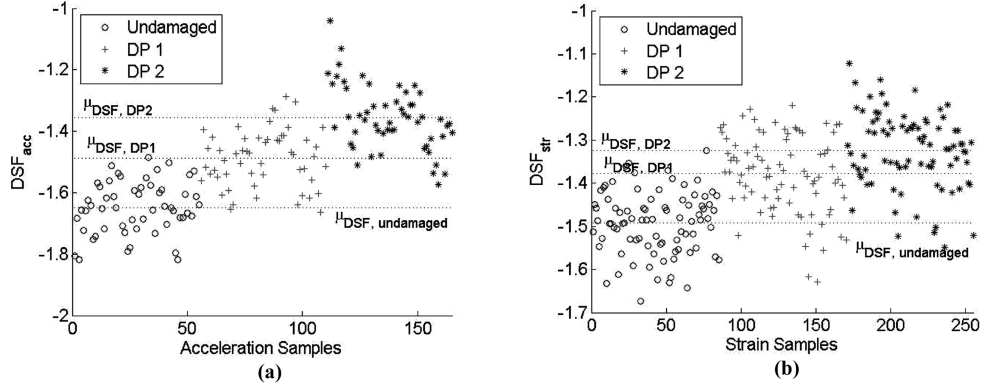


Fig. 6 Variation of DSF with damage: (a) Variation of $DSF_{acc,2}$ with acceleration samples; (b) Variation of DSF_{str} with strain samples. DP1 and DP2 correspond to Damage Case 1 and Damage Case 2, respectively

3.2.2. Classification using the t -statistic

Fig. 6 shows the AR coefficients for the undamaged, DP1 and DP2 for the acceleration and the strain signals. In the same figure the mean values of the DSF 's obtained from the damaged and undamaged cases are also shown. Denoting $\mu_{DSF,d}$ and $\mu_{DSF,u}$ as the mean values of the DSF 's obtained from the damaged and undamaged case, respectively, the hypothesis test for the significance in their values is set up as follows:

$$\begin{aligned} H_0: \mu_{DSF,u} &= \mu_{DSF,d} \\ H_1: \mu_{DSF,u} &\neq \mu_{DSF,d} \end{aligned} \quad (6)$$

where H_0 and H_1 are the null and alternate hypotheses, respectively. H_0 represents the undamaged condition and H_1 represents the damaged condition. The significance level of the test is set at 0.05. The hypothesis used in Eq. (6) is called a two-sided alternative.

For testing the above hypothesis, the t -statistic is used (Rice 1999). The damage decision is made by examining the point estimate and the confidence interval of the difference in the values of $\mu_{DSF,d}$ and $\mu_{DSF,u}$. The t -statistic is defined as follows:

$$t = \frac{\hat{\mu}_{DSF,u} - \hat{\mu}_{DSF,d}}{s \sqrt{\frac{1}{n} + \frac{1}{m}}} \quad (7)$$

where m and n are the number of samples obtained from DSF_d and DSF_u , respectively; and s is the pooled sample variance, given as:

$$s^2 = \frac{(n-1)S_{DSF,u}^2 + (m-1)S_{DSF,d}^2}{m+n-2} \quad (8)$$

where S^2 is the sample variance. The confidence interval for the difference in $\mu_{DSF,u}$ and $\mu_{DSF,d}$ is given as:

$$CI = (\hat{\mu}_{DSF,u} - \hat{\mu}_{DSF,d}) \pm t_{m+n-2} \left(\frac{\alpha}{2} \right) s \sqrt{\frac{1}{n} + \frac{1}{m}} \quad (9)$$

where $t_{n+m-2}(\alpha/2)$ is the value of the t -distribution with $n+m-2$ degrees of freedom obtained at $\alpha/2$.

3.3. Algorithm 2

3.3.1. Feature extraction

In this algorithm, the first three AR coefficients are defined as the feature vector as following:

$$\text{Feature Vector} = \begin{bmatrix} \alpha_1 \\ \alpha_2 \\ \alpha_3 \end{bmatrix} \quad (10)$$

where α_i is the i^{th} AR coefficient. The first three AR coefficients are chosen because they contain most of the information in the signals.

The feature vectors of the pre and post damage signals are modeled as separate Gaussian mixtures. A GMM with K classes (or mixtures) has the following form:

$$f(\mathbf{x}_{1:L}) = \sum_{i=1}^K \pi_i \varphi_i(\mathbf{X}; \theta_i) \quad (11)$$

where \mathbf{X} is the collection of L training feature vectors, $\varphi_i \sim N(\boldsymbol{\mu}_i, \Sigma_i)$ is a Gaussian vector with mean vector $\boldsymbol{\mu}_i$ and covariance matrix Σ_i and π_i is the non-negative mixture weight for each class (Nair, *et al.* 2006). By the assumption that the feature vectors of the pre and post damage signals are from different Gaussian mixtures, the number of classes and the mixture weights for each class are also determined. The rest of the unknown parameters of GMM, $\boldsymbol{\mu}_i$ and Σ_i , can be calculated in the following way:

$$\boldsymbol{\mu}_i = \frac{\sum_{j=1}^l \mathbf{x}_j}{l}$$

$$\Sigma_i = \frac{\sum_{j=1}^l (\mathbf{x}_j - \boldsymbol{\mu}_i)(\mathbf{x}_j - \boldsymbol{\mu}_i)^T}{l-1} \quad (12)$$

where l is the number of the feature vectors in the mixture i , and \mathbf{x}_j is the feature vector j in the mixture. The Gaussian mixture of the pre-damage signal is used as a baseline, and that of the post-damage signal is compared with the baseline using the Mahalanobis distance in order to determine the damage status.

3.3.2. Classification using Mahalanobis distance

In general, the Mahalanobis distance is a distance measure between two random vectors of the same distribution. It represents the dissimilarity between the two vectors considering the correlations between the components of the random vectors, and can be quantified as following:

$$\Delta(\mathbf{x}, \mathbf{y}; \Sigma) = \sqrt{(\mathbf{x} - \mathbf{y})^T \Sigma^{-1} (\mathbf{x} - \mathbf{y})} \quad (13)$$

where Σ is a covariance matrix. In this paper, the vectors \mathbf{x} and \mathbf{y} correspond to the mean values of the

feature vectors obtained from the baseline and the damaged signals, $\boldsymbol{\mu}_u$ and $\boldsymbol{\mu}_d$ respectively.

We define distance measures similar to the Mahalanobis distance, but the feature vectors of the pre and post damage signals are assumed to be from two different distributions. The Mahalanobis distance assumes that both feature vectors obtained from pre and post damage signals share the same covariance matrix, which is not true in practice. Thus, several different distance measures are defined utilizing different covariance matrix and used to determine their correlation to the various damage levels. They are defined as follows:

$$\Delta_1(\boldsymbol{\mu}_u, \boldsymbol{\mu}_d; \Sigma) = \sqrt{(\boldsymbol{\mu}_u - \boldsymbol{\mu}_d)^T \Sigma_u^{-1} (\boldsymbol{\mu}_u - \boldsymbol{\mu}_d)} \quad (14a)$$

$$\Delta_2(\boldsymbol{\mu}_u, \boldsymbol{\mu}_d; \Sigma) = \sqrt{|(\boldsymbol{\mu}_u - \boldsymbol{\mu}_d)^T \Sigma_{ud}^{-1} (\boldsymbol{\mu}_u - \boldsymbol{\mu}_d)|} \quad (14b)$$

$$\Delta_3(\boldsymbol{\mu}_u, \boldsymbol{\mu}_d; \Sigma) = \sqrt{(\boldsymbol{\mu}_u - \boldsymbol{\mu}_d)^T \Sigma_{u-d}^{-1} (\boldsymbol{\mu}_u - \boldsymbol{\mu}_d)} \quad (14c)$$

$$\Delta_4(\boldsymbol{\mu}_u, \boldsymbol{\mu}_d; \Sigma) = \sqrt{\left(\Sigma_u^{-\frac{1}{2}} \boldsymbol{\mu}_u - \Sigma_u^{-\frac{1}{2}} \boldsymbol{\mu}_d \right)^T \Sigma_u^{-\frac{1}{2}} \left(\boldsymbol{\mu}_u - \Sigma_u^{-\frac{1}{2}} \boldsymbol{\mu}_d \right)} = \sqrt{\boldsymbol{\mu}_u^T \Sigma_u^{-1} \boldsymbol{\mu}_u + \boldsymbol{\mu}_d^T \Sigma_d^{-1} \boldsymbol{\mu}_d - 2 \boldsymbol{\mu}_u^T \Sigma_d^{-\frac{1}{2}} \Sigma_u^{-\frac{1}{2}} \boldsymbol{\mu}_d} \quad (14d)$$

$$\Delta_5(\boldsymbol{\mu}_u, \boldsymbol{\mu}_d; \Sigma) = \sqrt{\frac{(\boldsymbol{\mu}_u - \boldsymbol{\mu}_d)^T \Sigma_u^{-1} (\boldsymbol{\mu}_u - \boldsymbol{\mu}_d)}{\boldsymbol{\mu}_u^T \Sigma_u^{-1} \boldsymbol{\mu}_u}} \quad (14e)$$

where

$$\Sigma_u = \frac{\sum_{j=1}^l (\mathbf{x}_j - \boldsymbol{\mu}_u)(\mathbf{x}_j - \boldsymbol{\mu}_u)^T}{l-1}, \quad \Sigma_d = \frac{\sum_{j=1}^l (\mathbf{y}_j - \boldsymbol{\mu}_d)(\mathbf{y}_j - \boldsymbol{\mu}_d)^T}{l-1}$$

$$\Sigma_{ud} = \frac{\sum_{j=1}^l (\mathbf{x}_j - \boldsymbol{\mu}_u)(\mathbf{y}_j - \boldsymbol{\mu}_d)^T}{l-1}, \quad \Sigma_{u-d} = \frac{\sum_{j=1}^l ((\mathbf{x}_j - \mathbf{y}_j)(\boldsymbol{\mu}_u - \boldsymbol{\mu}_d))((\mathbf{x}_j - \mathbf{y}_j)(\boldsymbol{\mu}_u - \boldsymbol{\mu}_d))^T}{l-1},$$

is the number of the feature vectors in the mixture, and \mathbf{x}_j and \mathbf{y}_j are the feature vectors j of the undamaged and damaged data, respectively. Δ_1 follows the fundamental definition of the Mahalanobis distance and is defined under the assumption that the distribution of the post damage feature vectors \mathbf{y} is similar to that of the pre damage feature vectors \mathbf{x} and the covariance matrix of the pre-damage state is used to weigh the distance between two vectors. Δ_2 uses the covariance matrix of \mathbf{x} and \mathbf{y} as the representative covariance matrix of the distributions of \mathbf{x} and \mathbf{y} . Thus, it includes the uncertainty of both the pre and post damage signals. Δ_3 uses the covariance matrix of the difference between the mean values of the pre damage feature vector \mathbf{x} and the post damage feature vector \mathbf{y} to weigh the distance. Δ_4 is derived from the definition of the Mahalanobis distance with the assumption that the covariance matrix of \mathbf{x} and \mathbf{y} are different. Δ_5 is the distance measure used by Nair and Kiremidjian (2007), which is the normalized Mahalanobis distance. Using the definitions above, the distances between the pre and post damage feature vectors are computed. For reference, the distance measures between the pre damage feature vectors are also computed. In order to compute them, the feature vectors for the undamaged case are divided into two groups by separating the even samples and the odd samples. The distance between the two groups is supposed to be theoretically zero. The results are discussed in the following section.

4. Damage diagnosis results

4.1. Algorithm 1

4.1.1. Acceleration data analysis

Tables 3 to 14 show the results of the t -test for the AR model and the confidence intervals for the difference in the mean values of the damaged and undamaged cases. The two DSF_{acc} defined by Eq. (4) were considered first for analysis of the acceleration data. It was found that $DSF_{acc,2}$ works well for damage detection, but does not effectively distinguish between DP1 and DP2. $DSF_{acc,1}$ results in smaller confidence intervals, but is able to distinguish DP1 from DP2. Tables 3 and 4 show the damage detection results using $DSF_{acc,1}$ for the unidirectional excitation with a peak amplitude of 60 gals, Tables

Table 3 Results of damage detection using $DSF_{acc,1}$ for 60 gal unidirectional random excitation for DP1 using the point estimate and CI of $\mu_{DSF,undamaged} - \mu_{DSF,DP1}$

Sensor no.	Damage decision	Point estimate	Confidence interval
A1a	H_0	0.0010	[-0.0107, 0.0127]
A3a	H_0	-0.0010	[-0.0141, 0.0121]
A1b	H_0	0.0092	[-0.0013, 0.0196]
A3b	H_0	0.0011	[-0.0105, 0.0126]
AY3a	H_0	0.0108	[-0.0185, 0.0400]
AY1b	H_0	-0.0014	[-0.0095, 0.0068]
AY2b	H_0	0.0257	[-0.0039, 0.0553]
AY3b	H_0	0.0114	[-0.0188, 0.0416]

Table 4 Results of damage detection using $DSF_{acc,1}$ for 60 gal unidirectional random excitation for DP2 using the point estimate and CI of $\mu_{DSF,undamaged} - \mu_{DSF,DP1}$

Sensor no.	Damage decision	Point estimate	Confidence interval
A1a	H_1	0.0223	[0.0105, 0.0340]
A3a	H_0	0.0002	[-0.0137, 0.0141]
A1b	H_1	0.0196	[0.0102, 0.0289]
A3b	H_0	0.0101	[-0.0010, 0.0211]
AY3a	H_1	-0.0433	[-0.0755, -0.0111]
AY1b	H_1	0.0203	[0.0115, 0.0290]
AY2b	H_0	-0.0300	[-0.0603, 0.0004]
AY3b	H_0	-0.0227	[-0.0552, 0.0098]

Table 5 Results of damage detection using $DSF_{acc,1}$ for 100 gal unidirectional random excitation for DP1 using the point estimate and CI of $\mu_{DSF,undamaged} - \mu_{DSF,DP1}$

Sensor no.	Damage decision	Point estimate	Confidence interval
AY2a	H_1	-0.0224	[-0.0329, -0.0118]
AY3a	H_1	-0.0428	[-0.0622, -0.0234]
AY1b	H_1	0.0185	[0.0120, 0.0249]
AY2b	H_1	-0.0253	[-0.0345, -0.0160]
AY3b	H_1	-0.0554	[-0.0773, -0.0334]

Table 6 Results of damage detection using $DSF_{acc,1}$ for 100 gal unidirectional random excitation for DP2 using the point estimate and CI of $\mu_{DSF,undamaged} - \mu_{DSF,DP2}$

Sensor no.	Damage decision	Point estimate	Confidence interval
AY2a	H_1	-0.0538	[-0.0687, -0.0388]
AY3a	H_1	-0.0668	[-0.0877, -0.0458]
AY1b	H_1	0.0429	[0.0367, 0.0491]
AY2b	H_1	-0.0665	[-0.0825, -0.0505]
AY3b	H_1	-0.1038	[-0.1288, -0.0787]

Table 7 Results of damage detection using $DSF_{acc,1}$ for 50 gal bi-directional random excitation for DP1 using the point estimate and CI of $\mu_{DSF,undamaged} - \mu_{DSF,DP1}$

Sensor no.	Damage decision	Point estimate	Confidence interval
A1a	H_1	0.0299	[0.0211, 0.0387]
A2a	H_1	0.0079	[0.0020, 0.0137]
A3a	H_1	-0.0134	[-0.0218, -0.0050]
A1b	H_1	0.0223	[0.0123, 0.0322]
A3b	H_0	-0.0050	[-0.0137, 0.0038]
AY1a	H_1	0.0206	[0.0134, 0.0278]
AY2a	H_1	0.0102	[0.0041, 0.0163]
AY3a	H_0	0.0048	[-0.0015, 0.0111]
AY1b	H_1	0.0315	[0.0238, 0.0392]
AY2b	H_0	0.0041	[-0.0025, 0.0107]
AY3b	H_0	0.0001	[-0.0058, 0.0060]

Table 8 Results of damage detection using $DSF_{acc,1}$ for 50 gal bi-directional random excitation for DP2 using the point estimate and CI of $\mu_{DSF,undamaged} - \mu_{DSF,DP2}$

Sensor no.	Damage decision	Point estimate	Confidence interval
A1a	H_1	0.0452	[0.0364, 0.0540]
A2a	H_0	0.0045	[-0.0016, 0.0105]
A3a	H_0	-0.0079	[-0.0164, 0.0006]
A1b	H_1	0.0445	[0.0341, 0.0549]
A3b	H_0	-0.0058	[-0.0138, 0.0023]
AY1a	H_1	0.0257	[0.0182, 0.0331]
AY2a	H_1	0.0180	[0.0118, 0.0241]
AY3a	H_0	0.0051	[-0.0016, 0.0118]
AY1b	H_1	0.0441	[0.0353, 0.0529]
AY2b	H_0	0.0053	[-0.0018, 0.0123]
AY3b	H_0	0.0034	[-0.0031, 0.0098]

5 and 6 show the damage detection results for the unidirectional excitation with a peak amplitude of 100 gals, and Tables 7 and 8 show the results for the bi-directional excitation with a peak amplitude of 50 gals. Tables 9 through 14 show the results using $DSF_{acc,2}$ for the unidirectional excitation with a peak amplitude of 60 gals and 100 gals and for the bi-directional excitation with a peak amplitude of 50 gals. The sensor locations are listed in the first column of the tables. Fig. 7 shows the point estimates of

Table 9 Results of damage detection using $DSF_{acc,2}$ for 60 gal unidirectional random excitation for DP1 using the point estimate and CI of $\mu_{DSF, undamaged} - \mu_{DSF, DP1}$

Sensor no.	Damage decision	Point estimate	Confidence interval
A1a	H_1	0.0569	[0.0029, 0.1109]
A3a	H_0	0.0123	[-0.0218, 0.0463]
A1b	H_0	-0.0111	[-0.0582, 0.0361]
A3b	H_0	-0.0019	[-0.0369, 0.0331]
AY3a	H_1	0.0590	[0.0129, 0.1050]
AY1b	H_1	0.0730	[0.0192, 0.1268]
AY2b	H_1	0.0636	[0.0076, 0.1195]
AY3b	H_1	0.0490	[0.0028, 0.0951]

Table 10 Results of damage detection using $DSF_{acc,2}$ for 60 gal unidirectional random excitation for DP2 using the point estimate and CI of $\mu_{DSF, undamaged} - \mu_{DSF, DP2}$

Sensor no.	Damage decision	Point estimate	Confidence interval
A1a	H_0	-0.0481	[-0.1008, 0.0046]
A3a	H_0	0.0143	[-0.0220, 0.0506]
A1b	H_1	-0.0725	[-0.1157, -0.0292]
A3b	H_0	0.0159	[-0.0191, 0.0509]
AY3a	H_0	-0.0227	[-0.0653, 0.02]
AY1b	H_1	-0.0857	[-0.1371, -0.0342]
AY2b	H_1	-0.0607	[-0.1118, -0.0096]
AY3b	H_0	-0.0386	[-0.0800, 0.0029]

Table 11 Results of damage detection using $DSF_{acc,2}$ for 100 gal unidirectional random excitation for DP1 using the point estimate and CI of $\mu_{DSF, undamaged} - \mu_{DSF, DP1}$

Sensor no.	Damage decision	Point estimate	Confidence interval
AY2a	H_1	0.1665	[0.1301, 0.2030]
AY3a	H_1	0.1234	[0.0842, 0.1626]
AY1b	H_1	0.1603	[0.1268, 0.1937]
AY2b	H_1	0.1301	[0.0925, 0.1676]
AY3b	H_1	0.1532	[0.1133, 0.1932]

Table 12 Results of damage detection using $DSF_{acc,2}$ for 100 gal unidirectional random excitation for DP2 using the point estimate and CI of $\mu_{DSF, undamaged} - \mu_{DSF, DP2}$

Sensor no.	Damage decision	Point estimate	Confidence interval
AY2a	H_1	0.2989	[0.2578, 0.3400]
AY3a	H_1	0.2093	[0.1713, 0.2473]
AY1b	H_1	0.2926	[0.2566, 0.3287]
AY2b	H_1	0.2379	[0.1962, 0.2797]
AY3b	H_1	0.2645	[0.2275, 0.3016]

$|\hat{\mu}_{DSF, u} - \hat{\mu}_{DSF, d}|$ using $DSF_{acc,1}$, and Fig. 8 shows those using $DSF_{acc,2}$.

The following conclusions are drawn from the analyses of the $DSF_{acc,1}$:

Table 13 Results of damage detection using $DSF_{acc,2}$ for 50 gal bi-directional random excitation for DP1 using the point estimate and CI of $\mu_{DSF,undamaged} - \mu_{DSF,DP1}$

Sensor no.	Damage decision	Point estimate	Confidence interval
A1a	H_0	0.0119	[-0.0193, 0.0432]
A2a	H_1	-0.1111	[-0.1465, -0.0758]
A3a	H_0	-0.0181	[-0.0473, 0.0109]
A1b	H_0	0.0248	[-0.0093, 0.0588]
A3b	H_0	0.0078	[-0.0224, 0.0381]
AY1a	H_0	-0.0307	[-0.0624, 0.0009]
AY2a	H_1	-0.0601	[-0.0925, -0.0277]
AY3a	H_0	-0.0334	[-0.0713, 0.0034]
AY1b	H_1	-0.0434	[-0.0736, -0.0131]
AY2b	H_1	-0.0429	[-0.0751, -0.0107]
AY3b	H_0	-0.0041	[-0.0394, 0.0311]

Table 14 Results of damage detection using $DSF_{acc,2}$ for 50 gal bi-directional random excitation for DP2 using the point estimate and CI of $\mu_{DSF,undamaged} - \mu_{DSF,DP2}$

Sensor no.	Damage decision	Point estimate	Confidence interval
A1a	H_1	-0.0745	[-0.1042, -0.0448]
A2a	H_1	-0.12843	[-0.1623, -0.0946]
A3a	H_1	-0.0489	[-0.0786, -0.0193]
A1b	H_1	-0.0742	[-0.1059, -0.0424]
A3b	H_1	-0.0285	[-0.0566, -0.0003]
AY1a	H_1	-0.0872	[-0.1214, -0.0529]
AY2a	H_1	-0.1412	[-0.1744, -0.1079]
AY3a	H_1	-0.0497	[-0.0890, -0.0103]
AY1b	H_1	-0.1107	[-0.1464, -0.0749]
AY2b	H_1	-0.0804	[-0.1171, -0.0437]
AY3b	H_0	-0.0166	[-0.0523, 0.0190]

• In the case of unidirectional random excitation with a peak amplitude of 60 gals, DP1 is not detected at any of the sensor locations while DP2 is detected at 4 out of 8 sensor locations using the t-statistic. As shown in Fig. 7 (a) and (b), the point estimates of $|\hat{\mu}_{DSF,u} - \hat{\mu}_{DSF,d}|$ for DP2 are larger than those for DP1 except at 1 out of 8 sensor locations.

• When the 100 gal unidirectional random excitation is applied, both DP1 and DP2 are detected at all of the sensor locations using t-statistic. Also, the point estimates of $|\hat{\mu}_{DSF,u} - \hat{\mu}_{DSF,d}|$ for DP2 are larger than those for DP1 as shown in Fig. 7(c). Thus, $DSF_{acc,1}$ could potentially be used for developing a damage extent measure, however, testing with additional data will be needed before it can be applied widely.

• In the case of bidirectional random excitation with a peak amplitude of 50 gals, DP1 is detected at 7 out of 11 sensor locations, and DP2 is detected at 5 out of 11 sensor locations. As shown in Fig. 7(d) and (e), the point estimates of $|\hat{\mu}_{DSF,u} - \hat{\mu}_{DSF,d}|$ for DP2 are larger than those for DP1 except at 2 out of 11 sensor locations. Furthermore, the analysis shows the largest point estimates to be closest to the damaged area.

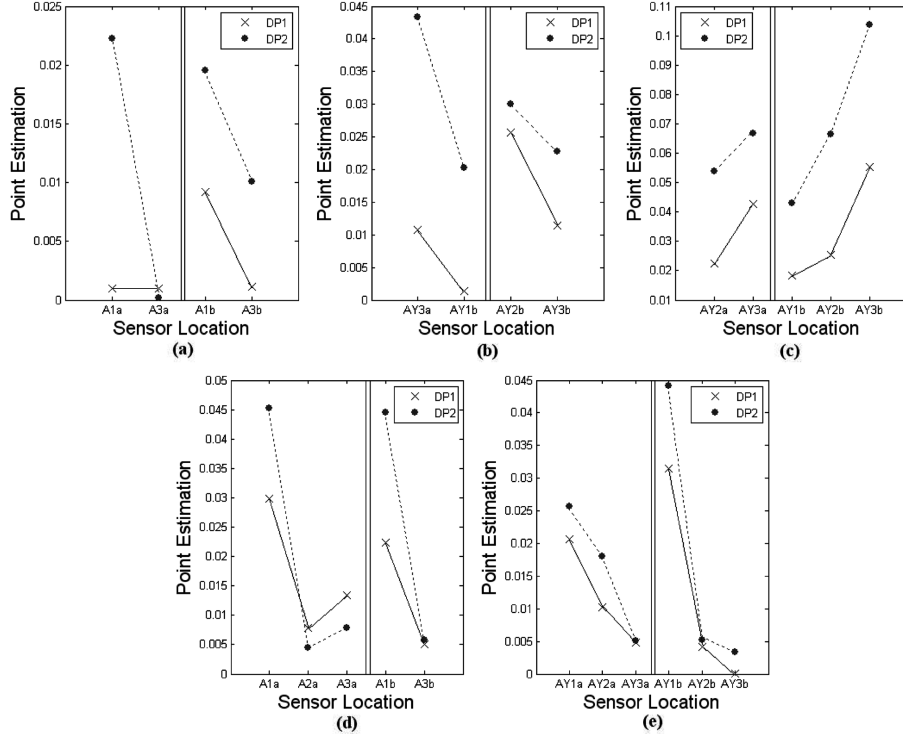


Fig. 7 point estimates of $|\hat{\mu}_{DSF,u} - \hat{\mu}_{DSF,d}|$ using $DSF_{acc,1}$: (a) 60 gal unidirectional random excitation, X direction data result; (b) 60 gal unidirectional random excitation, Y direction data result; (c) 100 gal unidirectional random excitation, Y direction data result; (d) 50 gal bidirectional random excitation, X direction data result; (e) 50 gal bidirectional random excitation, Y direction data result

For $DSF_{acc,2}$, the following observations are made:

- When the unidirectional random excitation with peak acceleration of 60 gal is applied to the structure, DP1 is detected at 5 out of 8 sensor locations while DP2 is detected at 3 out of 8 sensor locations using t -statistic.

- For the unidirectional random excitation with peak acceleration of 100 gal, damage was detected at all sensor locations. While this observation is encouraging that it enables us to identify damage, this DSF appears to be non-informative for damage localization purposes. As shown in Fig. 8(c) the point estimates of $|\hat{\mu}_{DSF,u} - \hat{\mu}_{DSF,d}|$ for DP2 are larger than those for DP1.

- When the 50 gal bidirectional random excitation is applied, DP1 is detected at 4 out of 11 sensor locations, and DP2 is detected at 10 out of 11 sensor locations. As shown in Fig. 8(d) and (e), the point estimates of $|\hat{\mu}_{DSF,u} - \hat{\mu}_{DSF,d}|$ for DP2 are larger than those for DP1.

Fig. 9 shows the damage measure DM , using $DSF_{acc,1}$, at each sensor for DP1 and DP2. The values of DM for DP2 are higher than that of DP1 demonstrating that this definition of DM appears to be sufficient to identify the relative magnitude of damage and can enable tracking of damage growth. Additional testing and analysis, however, is necessary to fully support this claim.

From the analysis described in this section, we can conclude that the difference between the mean of DSF 's for the undamaged and damaged structure increases when base excitation with larger peak acceleration is applied and more severe damage is introduced to the structure. For low intensity excitation,

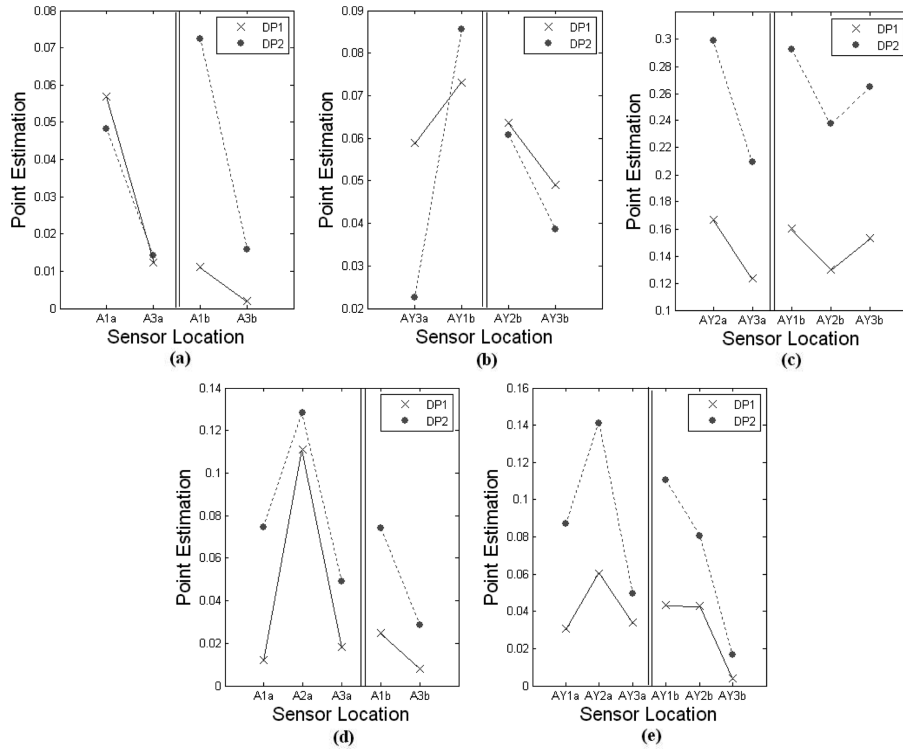


Fig. 8 point estimates of $|\hat{\mu}_{DSF,u} - \hat{\mu}_{DSF,d}|$ using $DSF_{acc,2}$: (a) 60 gal unidirectional random excitation, X direction data result; (b) 60 gal unidirectional random excitation, Y direction data result; (c) 100 gal unidirectional random excitation, Y direction data result; (d) 50 gal bidirectional random excitation, X direction data result; (e) 50 gal bidirectional random excitation, Y direction data result

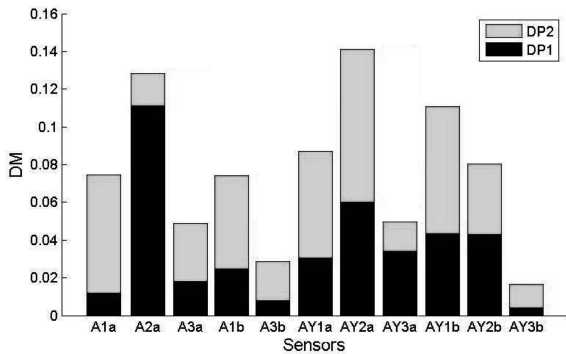


Fig. 9 DM of acceleration for bidirectional random excitation at each sensor location

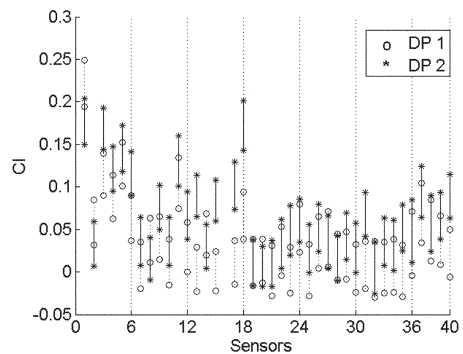


Fig. 10 Confidence intervals of the DSF_{str} for 50 gal bidirectional random excitation

such as the 60 gal unidirectional and 50 gal bi-directional input motions, damage is identified near the lower floors in close proximity to where indeed damage was introduced. However, testing with various minor damage patterns and real data has to be carried out and need to be pursued to further validate the algorithm.

4.2. Strain data analysis

Fig. 10 shows the values of the confidence intervals CI of the difference between the mean values of DSF of the strain data for the bidirectional random excitation with a peak acceleration of 50 gals.

As observed in Fig. 1, strain sensors S1-S6 are at the location of the cut on column 1 for DP1. Similarly for DP2, strain sensors S1-S6 and S13-S18 are at the location of the cut on columns 1 and 2 respectively.

From the analysis of strain data, the following observations are made:

- In the case of DP1, strain sensors S1 and S3 to S6 have larger values of CI 's as compared to other sensors. These sensors are close to the damaged area correctly pointing to the damage occurrence and its location.
- High values of CI are also observed for strain sensors S1, S3-S6 and S13-S18 in the case of DP2. Again these sensors are close to the damaged region on the structure.
- The CI 's for the higher floors are consistently lower than those at lower floors (Fig. 10). Thus localization of damage could potentially be achieved using the strain measurements. Again, additional studies and test cases need to be investigated to further reinforce this observation.

4.3. Algorithm 2

4.3.1. Acceleration signals

Fig. 11 shows Δ_1 of the acceleration data for the unidirectional random excitation (60 gal) for damaged and undamaged cases. It is observed that the undamaged cases and the damaged cases are hardly distinguishable. The magnitudes of the distance measure for pre and post damage signals are very close to one another, which indicate that the change in vibration response due to the damage is not significant. It is possible that unidirectional random excitation with the peak acceleration of 60 gal is not strong enough for us to detect the damage. An examination of the root mean square value of the response data resulted in values as high as 0.7 mg while the noise level of the recording instrument was 0.4 mg. Consequently, we feel that the instrument noise level was too high for reliable damage analysis.

When applying the second algorithm to the acceleration data for the unidirectional random excitation (100 gal), it is found that $\Delta_1, \Delta_2, \Delta_3,$ and Δ_5 have larger quantities at all the sensor locations for DP2 than

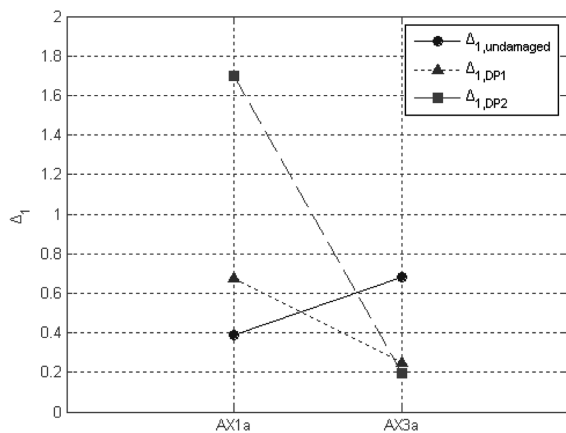


Fig. 11 Δ_1 of the acceleration data for 60 gal unidirectional random excitation X direction result at column (a)

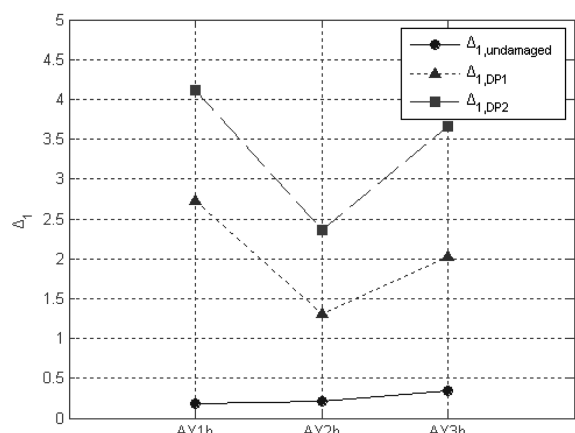


Fig. 12 Δ_1 of the acceleration data for 100 gal unidirectional random excitation Y direction result at column (b)

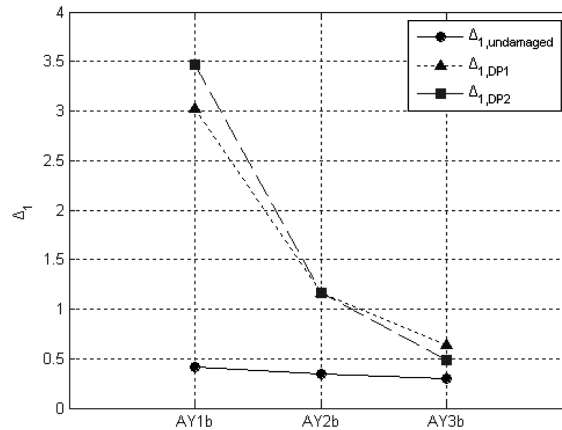


Fig. 13 Δ_1 of the acceleration data for 50 gal bidirectional random excitation Y direction result at column (b)

for DP1, which are in turn larger than for the undamaged case. Δ_4 has larger quantities for DP2 than for DP1, but those for the undamaged case are not always less than the damaged cases. Of all the measures listed in Eq. (14) Δ_4 least resembles a distance measure between the damaged and undamaged coefficients. As a result Δ_4 is not considered to be a suitable measure of damage. The distance measures are maximum on the first floor which is the closest floor from the damage and minimum on the second floor. The reason why the distance measure on the third floor is higher than the second floor might be due to the influence of higher modes that may be excited because of the asymmetry introduced by the damage at the base of the structure. Fig. 12 illustrates the distance measure Δ_1 of the acceleration data for the unidirectional random excitation (100 gal) for the damaged and undamaged cases.

Fig. 13 shows the distance measure Δ_1 of the acceleration data for the bidirectional random excitation (50 gal) for the damaged and undamaged cases. It is observed that the damaged cases have higher distance measures than the undamaged cases, but it is hard to distinguish between DP1 and DP2. It is possible that bidirectional random excitation with the peak acceleration of 50 gal is not strong enough for us to distinguish the two different damage patterns using this algorithm.

4.3.2. Strain signals

Tables 15 to 17 show the mean values of the distance measures of the strain data. Table 15 shows that the distance measures for the strain data for the unidirectional random excitation of 60 gal can distinguish the damaged cases from the undamaged case. It also shows that DP1 has higher distance measures than DP2 although DP2 is more severe damage case. These results again point to possible excessive noise in the response motions. Furthermore, the response motions are in the z -direction and would be most affected by input motions that are in the y -direction. The 60 gal motion is applied in the x -direction causing very small strains and consequently the values may be masked by possible noise in

Table 15 Results of mean values of various distance measures from the strain data for 60 gal uni-directional random excitation for undamaged and damaged cases

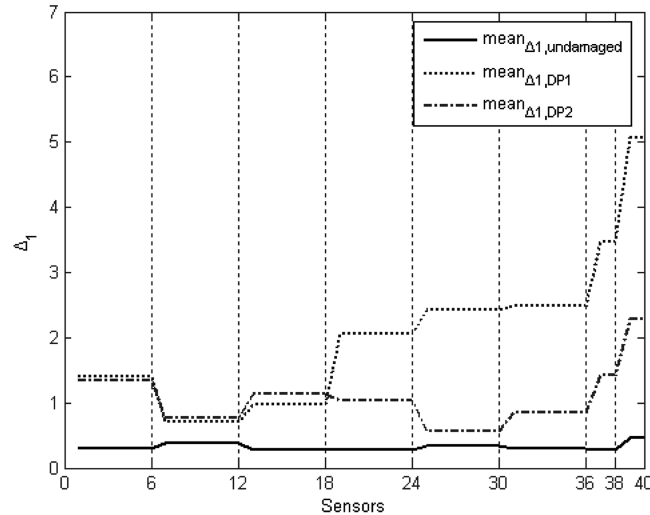
	Mean(Δ_1)	Mean(Δ_2)	Mean(Δ_3)	Mean(Δ_4)	Mean(Δ_5)
Undamaged	0.3003	0.7963	0.2653	3.4532	0.0114
DP1	1.9740	6.6970	1.5145	5.2080	0.0751
DP2	1.0650	3.3727	0.8110	4.5245	0.0413

Table 16 Results of mean values of various distance measures from the strain data for 100 gal uni-directional random excitation for undamaged and damaged cases

	Mean(Δ_1)	Mean(Δ_2)	Mean(Δ_3)	Mean(Δ_4)	Mean(Δ_5)
Undamaged	0.3468	0.8944	0.2632	8.8976	0.0095
DP1	0.9205	1.7466	0.9628	6.7689	0.0254
DP2	1.9404	6.8201	1.5201	10.1990	0.0502

Table 17 Results of mean values of various distance measures from the strain data for 50 gal bi-directional random excitation for undamaged and damaged cases

	Mean(Δ_1)	Mean(Δ_2)	Mean(Δ_3)	Mean(Δ_4)	Mean(Δ_5)
Undamaged	0.3559	0.8911	0.2477	8.6000	0.0074
DP1	0.7098	1.3376	0.7450	18.4979	0.0143
DP2	2.0007	6.2339	1.5005	15.6551	0.0391

Fig. 14 Mean values of Δ_1 of the strain data for 60 gal unidirectional random excitation shown in darker colors along the data

the sensors.

Tables 16 and 17 show that the distance measures for the strain data for the unidirectional random excitation of 100 gal and those for the bidirectional random excitation of 50 gal have smaller values for the undamaged cases than DP1, which are in turn smaller than DP2. Figures 14 to 16 show the mean values of the distance measure Δ_1 of the strain data at each location. The following observations are made from these figures:

- For the 100 gal and 50 gal peak acceleration excitation, the distance measure for DP2 has higher values than that for DP1.
- For the 100 gal and 50 gal peak acceleration excitation, the distance measure for DP1 has the maximum value at the damage location.
- For the 100 gal and 50 gal peak acceleration excitation, the distance measure for DP2 is higher for the higher floors.
- For the 60 gal peak acceleration excitation, the distance measure for DP1 is higher than that for DP2.

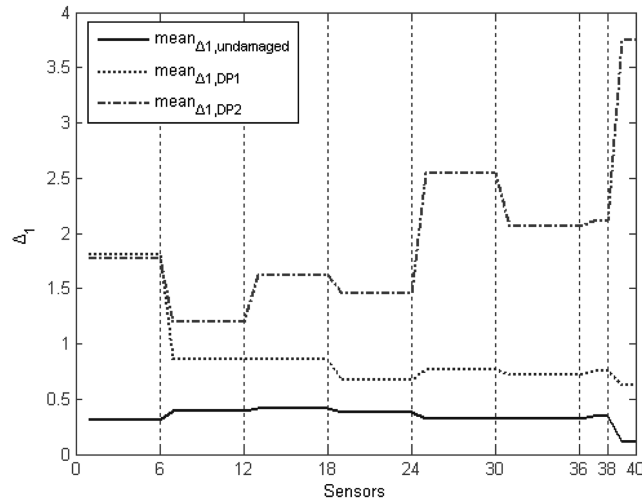


Fig. 15 Δ_1 of the strain data for 100 gal unidirectional random excitation

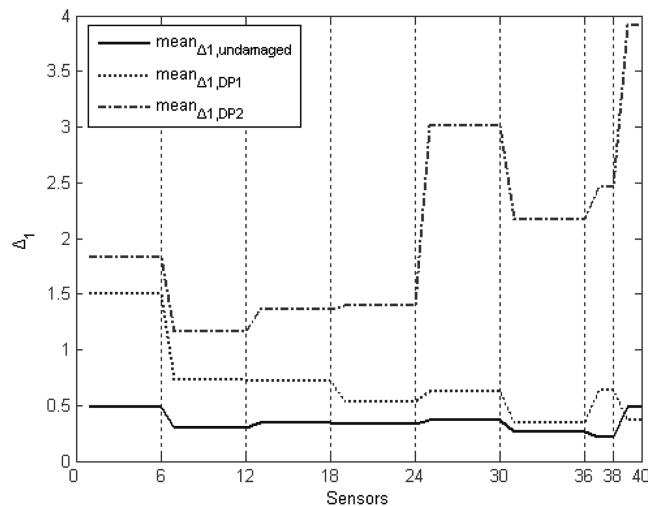


Fig. 16 Δ_1 of the strain data for 50 gal bidirectional random excitation

- For the 60 gal peak acceleration excitation, the distance measure for DP1 is higher for the higher floors.

5. Conclusions

This paper presents the results of the application of two time series-based damage detection algorithms (Nair, *et al.* 2006, Nair and Kiremidjian 2007) to the experimental data obtained from the Benchmark Structure of the National Taiwan University. Both acceleration and strain data from the wired system are analyzed. The vibration and strain signals are modeled as autoregressive (AR) and autoregressive time series with exogenous input (ARX). It is found that the AR model is sufficient to

capture the characteristics of both the acceleration and strain measurements and is thus adopted for damage discrimination. The data were tested to check the stability of the AR coefficients and it was found that the first AR coefficient changes by less than or about 5% with data samples of 200 or more. In addition, the time series were checked for stationarity and Gaussianity. These tests were performed only to measurements that were not corrupted. It was found in each of these tests that both the acceleration and the strain data are stationary and Gaussian. These data were then used in the subsequent damage analyses.

Several damage sensitive features were investigated, and the first three AR coefficients of the model are used to define the feature vector. In the first algorithm, which follows Nair, *et al.* (2006), a damage sensitive feature (*DSF*) is defined as a function of the first three AR coefficients for the acceleration, and the first AR coefficient is used for the strain data. Differences in the mean values of the *DSF* before and after damage indicate that there is damage in the structure and the t-test is used to evaluate the statistical significance of that difference. A damage measure *DM* is introduced based on the mean and variances of the *DSF*'s, and it is found that the *DM* can be directly correlated to the amount of damage in this simple application. In the second algorithm, which follows the developments of Nair and Kiremidjian (2007) a Gaussian Mixture Model (GMM) is used to characterize the feature vector. Damage diagnosis is achieved by determining the distance between the mixtures. The Mahalanobis distance, which is defined as the Euclidean distance between the mixtures weighted with respect to the inverse covariance matrix, as well as various other distance measures are used to quantify damage extent.

The results from the first algorithm presented in this paper show that the $DSF_{acc,2}$ can be used for damage detection; $DSF_{acc,1}$ and/or *DM* can be used for damage extent, and DSF_{str} can be used for damage localization. The results from the second algorithm show that the Mahalanobis distances for acceleration data and strain data can detect damage for 100 gal and 50 gal peak acceleration excitation, but not for 60 gal peak acceleration excitation. It is likely that unidirectional random excitation with the peak acceleration of 60 gal is not strong enough for us to detect the damage. It is found that the accelerometers used to measure structural response have a noise level that is of the same order as the root mean square of the measurements. Also, the Mahalanobis distances for acceleration data can be used to localize damage while the mean values of the distance measures of the strain data appears to be well correlated to damage extent.

Although the initial results of the analysis are promising, more testing needs to be performed. These should be for varying degrees of damage, loading conditions, environmental conditions such as temperature and humidity, as well as different sequences of damage occurrences. Different damage locations on the structure should be considered and damage sequences should also be investigated. It is only after extensive experimentation and field testing with calibration that these models can be widely applied. Never-the-less, the results presented in this paper are encouraging and represent good initial step towards achieving this goal.

Acknowledgments

The first author is supported by the Samsung Fellowship and their support is gratefully acknowledged. This research was partially supported by the NSF-NEESR Grant – 15BBK16379. We are also grateful to the National Center for Research in Earthquake Engineering for providing the test data used in this paper.

References

- Brockwell, P. J. and Davis, R. A. (2002), *Introduction to Time Series and Forecasting*, Springer-Verlag, Second Edition, New York.
- Chang, F-K. (ed.) (1999, 2001, 2003 and 2005), *1st, 2nd, 3rd and 4th International Workshops on Structural Health Monitoring*, Stanford University, Stanford, CA.
- Lynch, J. P., Wang, Y. Lu, K-C., Hou, T-C. and Loh, C-H. (2006), "Post-seismic damage assessment of steel structures instrumented with self-interrogating wireless sensors", *Proceedings of the 8th National Conference on Earthquake Engineering (8NCEE)*, San Francisco, CA.
- Nair, K. K., Kiremidjian, A. S. and Law, K. H. (2006), "Time series-based damage detection and localization algorithm with application to the ASCE benchmark structure", *J. Sound Vib.*, **291**(2), 349-368.
- Nair, K. K. and Kiremidjian, A. S. (2007), "Time series-based structural damage detection algorithm using gaussian mixtures modeling", *J. Dyn. Sys., Measurement, Control*, **129**, 285-293.
- Noh, H., Nair, K. K., Kiremidjian, A. S. and Loh, C-H. (2007), "Application of a time series-based damage detection algorithm to the taiwanese benchmark experiment", *Int. Conf. Appl. Statist. Probability in Civil Engineering*, CD Rom, Chiba, Japan. ISBN 978-0-415-45211-3.
- Rice, J. A. (1999), *Mathematical Statistics and Data Analysis*, Second Edition, Duxbury Press, Second Edition, New York.
- Sohn, H., Farrar, C. R., Hunter, H. F. and Worden, K. (2001), "Applying the LANL statistical pattern recognition paradigm for structural health monitoring to data from a surface-effect fast patrol boat", *Los Alamos National Laboratory Report LA-13761-MS*, Los Alamos National Laboratory, Los Alamos, NM 87545.